Volume 0 (1981), Number 0 pp. 1–17 COMPUTER GRAPHICS *forum*

Increasing the Spatial Resolution of BTF Measurement with Scheimpflug Imaging

V. Havran[†1] J. Hošek[2] S. Němcová[2] J. Čáp[2]

[1]Czech Technical University, Faculty of Electrical Engineering, Czech Republic
[2]Czech Technical University, Faculty of Mechanical Engineering, Czech Republic

Abstract

We present an improved way of acquiring spatially varying surface reflectance represented by a bidirectional texture function (BTF). Planar BTF samples are measured as images at several inclination angles which puts constraints on the minimum depth of field of cameras used in the measurement instrument. For standard perspective imaging we show that the size of a sample measured and the achievable spatial resolution are strongly interdependent and limited by diffraction at the lens' aperture. We provide a formula for this relationship. We overcome the issue of the required depth of field by using Scheimpflug imaging further enhanced by an anamorphic attachment. The proposed optics doubles the spatial resolution of images compared to standard perspective imaging optics. We built an instrument prototype with the proposed optics that is portable and allows for measurement on site. We show rendered images using the visual appearance measured by the instrument prototype.

CCS Concepts

•***Computing methodologies*** → ***Reflectance modeling;***

1. Introduction

The reproduction of real world appearance is indispensable for many scientific and industrial applications of computer graphics. This includes predictive rendering that allows for making the rendered images computed by the software indistinguishable from the real world. A natural method to represent surface reflectance accurately is to measure it by means of photographs from different viewing and illumination directions. This has received significant attention in the past as the rendered images should match to the real world counterparts as much as possible in applications such as movies and manufacturing industries producing expensive products. For a single point of a measured surface, the surface reflectance is represented as *bidirectional reflectance distribution function* (BRDF) as it was formalized by Nicodemus et al. [NRH*77]. It can be spatially extended over a part of surface to a *bidirectional texture function* [DVGNK99] (BTF). Unlike *spatially varying BRDF* (SVBRDF), BTF allows us to capture fine light interactions and non-local effects such as subsurface scattering, interreflection and self-shadowing on the mesoscopic and macroscopic scale. A BTF corresponds to a set of photographs of a measured sample surface parameterized by viewing and illumination directions, supposing that the illumination is realized by a collimated light source and photographs are taken with an orthographic camera. In practice, the orthographic camera is approximated with a standard perspective camera.

While the BTF formulation is simple, the methods of its acquisition, storing, and processing are relatively involved and time consuming. One reason is that a BTF represents a seven-dimensional function: two dimensions are needed to represent an illumination direction ω_i, the next two to represent a viewing direction ω_o, another two a spatial position of a texel in the plane s,t, and the one remaining is a wavelength. The measured quantity $\mathrm{BTF}(s,t,\omega_i,\omega_o,\lambda)$ represents a monochromatic image of a material sample for a surface point with coordinates (s,t) with illumination direction ω_i and viewing direction ω_o. The BTF is a continuous function over its domain that can be measured only in a discrete form by samples, i.e. photographs. The BTF is mostly acquired only for a tristimulus representation of spectra, i.e. in the RGB space of a trichromatic camera. For the application purposes such as rendering, the images measured during BTF acquisition are rectified.

A BTF that represents the visual appearance of a material sample surface requires thousands of photographs to be taken usually as high dynamic range images by using multiple exposures to achieve faithful visual appearance reproduction. The measurement of BTF is still far from being a standard method used in daily practice within various industries. A BTF is currently measured in experimental setups in only a few research facilities around the world, the majority of them requiring laboratory conditions.

† Corresponding author's e-mail: havran@fel.cvut.cz

Within the last two decades, great effort was put into the design and building of these BTF measurement setups to get a method usable in practice. Recently and also thanks to technological advancements, some BTF measurement setups reached a sufficient spatio-directional resolution and measurement time. Also, recent novel setups [FVK14, HHN*17a] allow for terrain measurement of BTF samples on site, without the necessity to extract samples from their surroundings and bring them to a stationary setup in a lab.

2. Overview

Below, we give an overview of this paper. First, we review the existing BTF measurement setups and their properties. Most of these instruments use standard perspective imaging to measure the reflected light from a sample. Therefore we analyze the BTF measurement with a standard perspective camera and show a limitation between a measured sample size (in mm) and spatial resolution (in pixels per mm or dots per inch) because the required *depth of field* (DoF) is substantial as the sample is viewed at a high tilt angle θ. While the DoF can be increased by closing the aperture, this is possible only to the point when the diffraction starts to play a role. We show that the DoF and spatial resolution are strongly interrelated and we provide an explicit formula for this relationship.

As a result, for a given sample size imposing DoF the spatial resolution achievable by standard perspective imaging is limited. To overcome this limitation we propose to make use of *Scheimpflug imaging* combined with *anamorphic imaging*. This combination naturally fits to the BTF measurement.

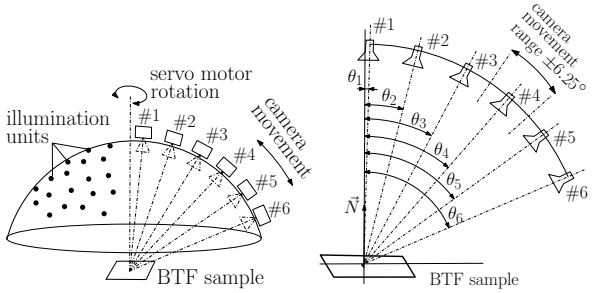

Figure 1: Lightdrum, base setup, (a) instrument outline, (b) notation of tilt angles θ for six cameras.

We demonstrate the proposed idea by its practical realization that allows for measurement on site. For realization we use the measurement setup published recently in [HHN*17a, HHN*17b], referred to as a *base setup*, and extend it by the proposed imaging optics. The concept of the base setup is outlined in Figure 1(a). The base setup uses standard perspective imaging for each of its six cameras that are used to take the images during measurement. The whole instrument resembles a drum of 600mm diameter and 400mm length. It includes cameras and illumination units mounted on an inner hemispherical dome. It is rotated by a geared servo motor over a sample. The outer frame with the servo motor allows the orientation of the instrument to a sample fixed in space.

The six cameras are mounted onto a circular arc that allows for an approximately circular motion within a small range of tilt angle $\pm 6.25^\circ$. Each camera has a different tilt angle towards the planar sample as shown in Figure 1(b). This way it is possible to orient a camera in any direction towards the measured sample in the range of tilt angle $\theta \in \langle 0^\circ, 75^\circ \rangle$.

In this paper we will propose the *extended setup* that is equipped with Scheimpflug imaging combined with anamorphic attachment. For the same range of tilt angle $\theta \in \langle 0^\circ, 75^\circ \rangle$ as the base setup we will get almost doubled spatial resolution. As the extended setup was realized we show the results in the form of raw measured images from the extended setup and also as the processed data used to render images. In summary, our contributions are:

- The mathematical analysis of DoF for standard perspective imaging, often applied in the computer graphics methods for data acquisition. We show that the existing setups are mostly diffraction limited.
- The analysis and design of a specialized perspective imaging based on the Scheimpflug principle enhanced by an anamorphic attachment. We show that it can double the spatial resolution.
- The practical realization of portable BTF measurement setup with the proposed enhanced optics.

3. Related Work

The BTF method of surface reflectance representation was proposed by Dana et al. [DNvGK97, DVGNK99] twenty years ago. For the introduction to this topic we refer to the recent surveys by Weinmann et al. [WK15], Schwartz et al. [SSW*14], Haindl and Filip [HF13] and Dana [Dan16]. Below, we describe briefly the existing BTF measurement setups and their categorization.

As the measurement of BTF is difficult due to data dimension and size, there are only a few realized BTF setups, all of them experimental and the majority of them working in laboratory conditions. Some research papers, including recent ones, limit the data acquisition to a spatially varying BRDF (SVBRDF) concept that assumes the Helmholtz reciprocity and severe sparsity of acquired data. Such approaches are described in [RPG16, AWL13, XDPT16, ZCD*16] and recently in the commercial product X-Rite [XR16]. The use of Helmholtz reciprocity, the assumption of data sparseness and the use of analytical BRDF models makes those methods inappropriate for BTF acquisition.

In general, all BTF measurement setups can be categorized briefly as photogonioreflectometer setups, dome based setups using a light stage principle, and various other setups. Portable BTF measurement setups are rare due to the difficulty of putting the luminarie(s) and sensor(s) into a small space, in particular, where the device is to be used for on-site measurement. Below, we survey the setups that could be realized as portable ones and some others closely related to these.

The first proposal for a portable instrument was outlined by Dana [Dan01] but it was never realized in practice to attain portability. It is based on an ellipsoidal mirror, a structured light source, and a beam splitter that separates the incident light from the reflected light. By moving the setup over a planar sample it was, in principle, possible to measure BTF. This setup proposal, unlike all others, uses a telecentric camera.

Another proposal allowing, in principle, a measurement on site also uses a tapered kaleidoscope. It was proposed by Han and Perlin [HP03] and uses a beam splitter to separate the illumination and viewing optical paths. The trapezoidal mirrors forming a tapered kaleidoscope allow for one or more reflections, featuring a directional dependence of viewing and illumination directions. The disadvantage of this setup is its low spatial and directional resolution. The setup was tested in laboratory conditions only.

The parallelization of data acquisition is allowed by camera array setups with cameras and a set of luminaries on the surface of a hemispherical dome or a part of it. A stationary setup for measuring 3D objects including a seated human, called a light stage, was proposed by Debevec at al. [DHT*00]. The measured object is put in the center of a hemisphere. A setup for sparse mobile BRDF measurement on site proposed by Ben-Ezra et al. [BEWW*08] uses a hemispherical dome that contains a set of LEDs. The LEDs were used both for the illumination and for the sensing of the light reflected from the sample. Malzbender et al. [MGW01] used the same idea for polynomial texture maps providing low resolution surface reflectance acquisition for a single camera at the surface normal direction. Further, Mueller et al. [MMS*05] used this principle and designed a stationary dome based setup for measuring BTF data. It contains 151 off-the-shelf cameras whose flash lights serve for illumination. This setup was extended by Schwartz et al. [SSWK13] by adding a rotary stage on which the measured sample is put. Then only 12 cameras, on a meridian stage, were needed. The last two dome based setups are movable but they require a re-calibration after transport. Further, they do not allow for measurement on site. Details are in the recent survey [SSW*14]. Further, Köhler et al. [KNRS13] proposed another fully spherical stationary setup with cameras mounted on a rotating arc. While all the setups surveyed above can be disassembled and can be called portable in principle, their size and the necessity for a re-calibration after reassembly makes on-site measurement impossible. Another possibly portable device with one camera and two light sources, hence with very limited directional resolution at the tilt angle, was proposed by Filip et al. [FVK14].

With all the approaches surveyed above, as published, it is unfortunately not possible to measure the surface reflectance represented as BTF on site while achieving high spatial and directional resolution. Some of those devices were constructed in such a way that they cannot be placed in an arbitrary position and orientation against a sample fixed in space. Some other devices, like the one by Filip et al. [FVK14], allow for only a rather limited directional resolution and they are not rigid enough mechanically to be positioned arbitrarily in space for practical measurement.

An approach to overcome these limitations was proposed recently by Havran et al. [HHN*17a], with the optomechanical design detailed by Hosek et al. [HHN*17b]. As this paper builds on this setup, it is described in more detail in Section 2.

4. Depth of Field for Standard Perspective Imaging

Almost all surface reflectance and in particular BTF measurement setups reviewed in the previous section use standard perspective imaging. Perspective imaging is the most commonly used optical arrangement for taking images in photography, computer graphics and computer vision applications. Perspective imaging was studied in the context of computer graphics for rendering algorithms in [HD14, KMH95]. For imaging applications, real optical systems with thick lenses are designed to have low aberrations. They achieve a high quality non-distorted imaging that ideally corresponds to a thin lens imaging.

4.1. Thin lens imaging

Below we review thin lens imaging with the geometry as depicted in Figure 2. We will use the Newtonian notation and Cartesian convention: distances are measured from focal points and they are oriented – negative to the left (or down for heights) and positive to the right (and up for heights). We combined the properties of thin lens imaging with diffraction on a circular aperture and derived the relationship between the depth of field and spatial resolution.

The symbols in Figure 2 have the following meaning: f (f')... focal length in object (image) space, note that $f = -f'$, x... object distance from front focal plane ($x < 0$), x'... image distance from back focal plane ($x' > 0$), A... farthest object point in focus at object distance x_A, B... nearest object point in focus at object distance x_B, x'_a and x'_b... image distances of corresponding points A and B projected to image space, Δ... size of sensor's pixel projected onto object ($\Delta > 0$), Δ'... pixel size on sensor ($\Delta' < 0$), D... aperture diameter, DoF... depth of field.

The Newtonian thin lens formula [DD08] relates the image distance x' to the object distance x:

$$xx' = -(f')^2 \tag{1}$$

Next, we use the lateral magnification expressed in Newtonian notation. It can be derived from the geometry of a ray passing the lens center using the triangular similarity and substituting for x from eq. 1:

$$\beta = \frac{\Delta'}{\Delta} = \frac{x' + f'}{x - f'} = \frac{-x'}{f'} \tag{2}$$

The formula holds only if $x' > 0$, which implies $x < 0$. If the lens is focused at the distance x and the diffraction at the aperture is not accounted for, the point in object space at distance x is represented as a point on the image plane at distance x'.

Moving the object from the plane in focus at distance x to a different distance y causes a point in object space to be projected onto the image plane as a circle of confusion with the diameter $S_F(y)$. The diameter $S_F(y)$ due to the defocus can be computed from triangular similarities in the image space for both extremal points x_B and x_A directly from Figure 2:

$$\frac{D}{f' + y'} = \frac{S_F(y)}{y' - x'} \quad \text{for } y' > x' \ \ldots \text{ i.e. } y' = x'_b \tag{3}$$

$$\frac{D}{f' + y'} = \frac{S_F(y)}{x' - y'} \quad \text{for } y' < x' \ \ldots \text{ i.e. } y' = x'_a \tag{4}$$

By substitution from eq. 1 for x' and y' we get the size of the circle of confusion $S_F(y)$ defined as a positive value ($S_F(y) \geq 0$):

$$S_F(y) = \frac{Df'}{x} \frac{y - x}{y - f'} \quad \text{for } y > x \ \ldots \text{ i.e. } y = x_B \tag{5}$$

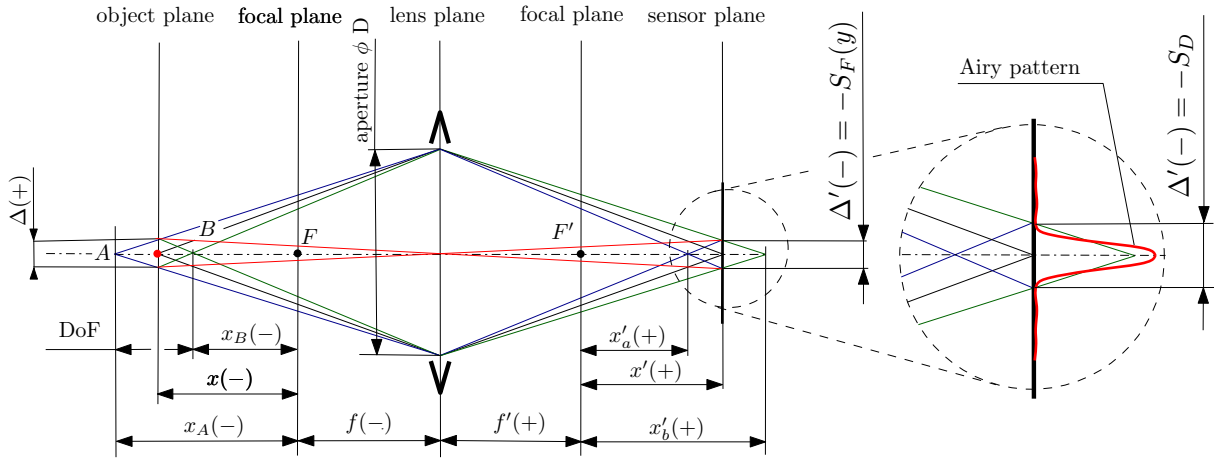

Figure 2: The geometry of thin lens imaging with a limited DoF for paraxial rays. Newtonian notation is used, i.e. object and image distances are measured from focal points.

$$S_F(y) = \frac{Df'}{x}\frac{x-y}{y-f'} \quad \text{for } y < x \ \ldots \text{ i.e. } y = x_A \tag{6}$$

The DoF denotes the range in the object space where the object is in focus, which means the size of the blurred spot $S_F(y)$ in the image space is less than or equal to the size of the sensor pixel Δ'. Because Δ' is negative this is expressed by the condition:

$$S_F(y) \leq -\Delta' \tag{7}$$

When the camera is focused at the distance x, there are two extremal points of focus A and B at the distances x_A and x_B ($x_A < x$, $x_B > x$). At these object distances the size of blurred spot $S_F(y)$ equals the size of the sensor pixel, so $S_F(x_A) = -\Delta'$ and $S_F(x_B) = -\Delta'$. Then we can express the DoF simply as the difference between these object distances, $\text{DoF} = x_B - x_A$.

4.2. Diffraction

The DoF denotes the range where the object is in focus, which means the diameter of the blurred spot due to defocus is less than the diagonal of the sensor pixel Δ'. The DoF can be increased by closing the lens aperture to decrease the size of defocus spot S_F. However, as the aperture diameter D gets smaller, *diffraction* at the edges of the aperture becomes more pronounced. Therefore, even with a perfect lens, the image of a single point is never a point but a diffraction spot, known as the Airy disc [Air34], introduced to computer graphics already in [PC81]. The size of blur S_D on the sensor due to diffraction on the circular aperture [Air34] depends proportionally on the distance of the sensor from the lens $(x' + f')$ and inversely to the aperture size as D as follows:

$$S_D = \frac{L}{D}(x' + f'), \tag{8}$$

where $L = 2.44\lambda$ and the mean wavelength $\lambda = 550\text{nm}$ is commonly used for computations in optical design. The constant 2.44 assumes we can provide an image of a sample pattern in the form of a black-white grid at the object plane to the camera sensor, ideally recognizable as a grid again, if we neglect the Moire pattern effect.

Indeed, there are two sources of blur on the image sensor: the first one due to defocus expressed by eqs. 5 and 6 (the blur is bigger for a bigger aperture D) and the second one due to diffraction expressed by eq. 8 (the blur is bigger for a smaller aperture D). In a balanced design of imaging optics the size of spots due to defocus and diffraction are equal so as to maximize the depth of field, i.e. $\max(S_D, S_F) \leq -\Delta'$ for any pixel of a sharply imaged object in the range of focus between x_A and x_B.

Example images showing blur caused by defocus and diffraction for the tilted sample are shown in Figure 3. Figure 4 shows a more pronounced diffraction effect and the resulting blur in an experiment with a standard photographic camera.

4.3. Depth of field as function of spatial resolution

Assuming the size of a sensor pixel projected onto the planar sample object Δ is in mm, the spatial resolution in *pixels per mm* or *lines per mm* in object space is then:

$$R = 1/\Delta \tag{9}$$

The spatial resolution R is often reported in *dots per inch* (DPI), thus as a value of $25.4R$. Below we adhere to standard SI units so to lines/mm while we provide the charts with functional dependences in alternative units in the supplementary. Further, we follow the notation in standard SI units.

The derivation of the resulting formula for DoF consists of three steps. As the first step, we prepare two equations for focal length f' and aperture diameter D. By substituing for Δ from eq. 9 to eq. 2 and removing x' using eq. 1 we get:

$$f' = xR\Delta' \tag{10}$$

From eq. 8 and eq. 1 we express the aperture diameter at the diffraction limit, so for condition $S_D = -\Delta'$:

$$D = \frac{L}{\Delta'}\left(\frac{(f')^2}{x} - f'\right), \tag{11}$$

(a) (b) (c)

Figure 3: Images of a sample taken at $x = 260$mm distance by camera PointGrey CM3-U3-31S4C-CS, Fujinon lens $f' = 12.5$mm, pixel size 3.45μm. (a) planar object viewed at the direction to surface normal ($\theta = 0^\circ$), *f-number* f/1.4 (the aperture diameter $D = 8.9$mm) – defocus blur starts to become visible, (b) the object viewed at angle $\theta = 60^\circ$ for the same *f-number* f/1.4, (c) object viewed at angle $\theta = 60^\circ$, *f-number* f/5.6 (the aperture diameter $D = 2.23$mm) – diffraction blur starts to become visible.

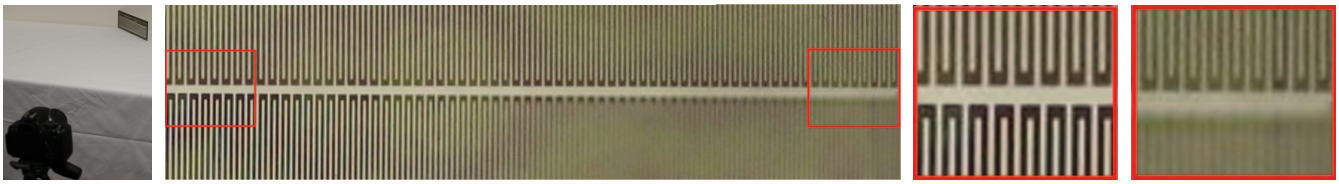

(a) (b) (c) (d)

Figure 4: (a) Experiment setup for camera and the planar object tilted against the optical axis. (b Top) The effect of the small aperture diameter. Closing the stop causes the diffraction to be more pronounced, image taken for *f-number* 22 (small aperture) makes diffraction visible for the whole image. (b Bottom) The camera is focused at a particular distance on the left of the image. The blur increases to the right as the object distance decreases causing the object to become out of focus. Image was taken for *f-number* 5.6 (large aperture). (c) Close-up of the left part of the images at (b). (d) Close-up of the right part of the images at (b).

By substitution of f' from eq. 10 into eq. 11 we formulate D as:

$$D = LxR(R\Delta' \quad 1) \tag{12}$$

As the second step we derive the DoF from eqs. 5 and 6 using distances x_A and x_B when a camera is focused at x, with the condition that the blur size equals the sensor pixel size (i.e. $S_F(y) = \quad \Delta'$):

$$x_A \;=\; f'x\frac{D \quad \Delta'}{f'D \quad \Delta'x} \quad \text{and} \quad x_B = f'x\frac{D+\Delta'}{f'D+\Delta'x} \tag{13}$$

We can then compute DoF as the difference between x_B and x_A:

$$\text{DoF} \;=\; x_B \quad x_A = f'x\left(\frac{D+\Delta'}{f'D+\Delta'x} \quad \frac{D \quad \Delta'}{f'D \quad \Delta'x}\right) \tag{14}$$

Because for any four variables M,N,O,P the following formula holds

$$\frac{M+N}{O+P} \quad \frac{M \quad N}{O \quad P} = \frac{2(NO \quad MP)}{O^2 \quad P^2},$$

we can then compute DoF by substitution: $M = D, N = \Delta', O = f'D$ and $P = \Delta'x$:

$$\text{DoF} \;=\; f'x\frac{2(\Delta' f'D \quad D\Delta'x)}{(f'D)^2 \quad (\Delta'x)^2} = \frac{2Df'x\Delta'(f' \quad x)}{(f'D)^2 \quad (\Delta'x)^2} \tag{15}$$

In the third step we get the final formula by combining the eq. 15 with the properties of diffraction. We substitute for D from eq. 12 and for f' from eq. 10. Then we simplify the equation by dividing both nominator and denominator by the term $(\Delta'x)^2$ and we get:

$$\begin{aligned}\text{DoF} \;&=\; \frac{2[LxR(R\Delta' \quad 1)][xR\Delta']x\Delta'(xR\Delta' \quad x)}{([xR\Delta'][LxR(R\Delta' \quad 1)])^2 \quad (\Delta'x)^2} \\ \text{DoF} \;&=\; \frac{2Lx^4R^2(\Delta')^2(R\Delta' \quad 1)^2}{(\Delta'x)^2(L^2R^4x^2(R\Delta' \quad 1)^2 \quad 1)}\end{aligned} \tag{16}$$

We can then express the resulting formula as follows:

$$\text{DoF} = \frac{2R^2x^2L(R\Delta' \quad 1)^2}{R^4x^2L^2(R\Delta' \quad 1)^2 \quad 1}, \tag{17}$$

The derived eq. 17 is new to the best of our knowledge and was not published before in any literature. We want to emphasize that the derivation is valid only for paraxial rays (those close to the optical axis) assuming thin lens imaging, i.e. perfect imaging. For real optics with thick lenses imposing more severe limitations the DoF can only be smaller or the spatial resolution can only be worse.

The requirement for the DoF in the context of BTF measurement is given by the size of the measured planar sample h and the maximum tilt angle θ_{max} (for example $\theta_{max} = 75^o$) between the

camera's optical axis and the observed flat surface's normal:

$$\mathrm{DoF} > h \sin \theta_{max} \tag{18}$$

We can then relate the spatial resolution R and the sample size h:

$$\mathrm{h} \leq \frac{2R^2x^2L(R\Delta'-1)^2}{(R^4x^2L^2(R\Delta'-1)^2-1)\sin\theta_{max}}, \tag{19}$$

where the object distance x and the pixel size Δ' on the detector are taken as constants. It can be shown numerically that the dependence of the eq. 19 on Δ' is negligible for a wide range of manufactured camera sensors, including 2×2 or 4×4 pixel binning, i.e. the range of pixel size $|\Delta'| \in \langle 0.001, 0.01\rangle$mm and object distance $x > 100$mm. Also, the dependence on object distance x is low for $x > 100$mm. Therefore we get the dependence between DoF and spatial resolution R. We provide a supplementary with MS Excel and GNUPLOT files to allow readers to experiment and study the data from the resulting equation 19.

Although the dependence of DoF on pixel size Δ' is negligible, the optical design is not finished by evaluation of the eq. 19 as a lens with focal length f' computed by eq. 10 and a sensor (its size h' and pixel size $|\Delta'|$) have to be selected from the many lenses and sensors available on the market so as to allow for imaging the whole object on the selected sensor. The sensor size h' has to be large enough to capture the whole planar sample of size h when viewed at normal direction. The lens distortion should be low and the lens quality should correspond to the sensor's image resolution. This is typically expressed as a lens for 1.5 or 5 MPixels etc. The aperture diameter D hence $f\text{-}number = f'/D$ should be computed from eq. 11. The signal to noise ratio (SNR) of the image captured by the sensor is influenced by several factors, including the $f\text{-}number$, the sensor pixel size Δ', the radiance intensity reflected from the sample towards the camera, and the sensitivity of the sensor. The whole discussion for the optical design completion is out of the scope of this supplementary and is discussed widely in the literature, e.g. [DD08]. The straightforward way to improve SNR is to increase the intensity of the illumination units used in the measurement instrument. The intensity of illumination in our instrument can be increased 20 times by changing the current of the LEDs but this was not necessary as the maximum exposure time for acquisition of HDR images was below 10ms.

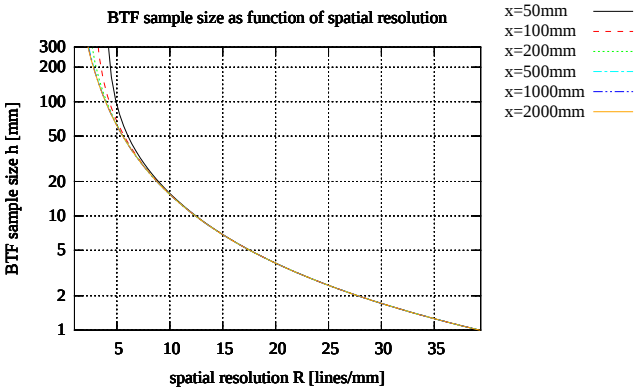

(a) range of spatial resolution $R \in \langle 0, 40\rangle$ lines/mm

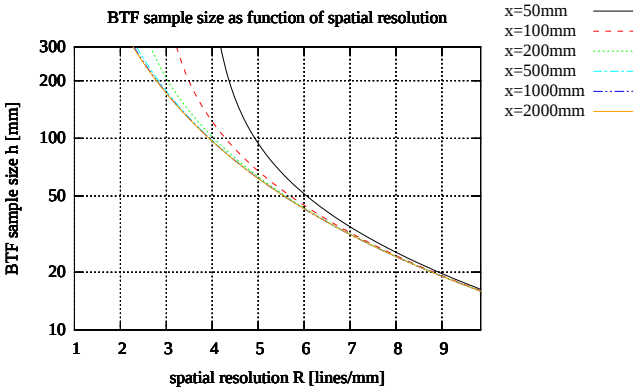

(b) range of spatial resolution $R \in \langle 1, 10\rangle$ lines/mm

Figure 5: The functional dependence of maximum BTF sample size h on the spatial resolution R (in lines/mm) for the whole object to be in focus and $\theta_{max} = 75°$, for five distances of object plane to the focal plane x for the range (a) $R \in \langle 0, 40\rangle$ lines/mm (b) $R \in \langle 1, 10\rangle$ lines/mm. The pixel size was $|\Delta'| = 0.0025$mm, the dependence on Δ' cannot be distuinguished for commonly used size of sensor pixel in range $|\Delta'| \in \langle 0.001, 0.01\rangle$mm and object distance $x > 100$mm.

4.4. Discussion

The dependence of sample size h as a function of spatial resolution R with three constants x, Δ', and $\theta_{max} = 75°$ is shown in Figure 5. The dependence of h on θ_{max} is by a constant only. The dependence of DoF on x becomes negligible for higher spatial resolution R as is clear from the analysis of eq. 19 and also documented in Figure 5. When a higher spatial resolution for a fixed sample size is required it is necessary to decrease the distance of the camera to the sample. This limits the construction of any measurement instrument with perspective imaging as the illumination unit and the camera with lens used in the measurement must not collide with each other. From Figure 5 the meaning of eq. 19 is: any increase of the spatial resolution R requires a decrease of the sample size h.

It could be also postulated in another way – as a utility measure $\chi(x,h)$ of the measurement instrument. We define it to be linearly proportional to the number of sharply imaged points on the planar object projected on a camera sensor as pixels and inversely proportional to the object distance $(-x)$ and camera viewing angle α because the smaller instrument the better and the viewing angle should be optimally close to zero. The camera viewing angle could be roughly approximated by $\alpha \approx \frac{h}{-x}$ for smaller angles because $\tan(\alpha) \approx \alpha$ for $\alpha < 15°$. Then we get the utility measure as:

$$\chi(x,h) = \frac{(hR(x,h))^2}{(-x\alpha)} = \frac{(hR(x,h))^2}{-x2\tan^{-1}(\frac{h/2}{-x})} \approx R^2(x,h)h \tag{20}$$

When we use this instrument utility measure, we get almost a constant, irrespective of R, h and x, as shown in Figure 6 for small viewing angles ($\alpha < 15°$). The instrument utility measure can be interpreted as: for a planar rectangle of size $1 \times h$ the number of points on the rectangle that can be viewed sharply by a camera is almost a constant, irrespective of h and the (object) distance be-

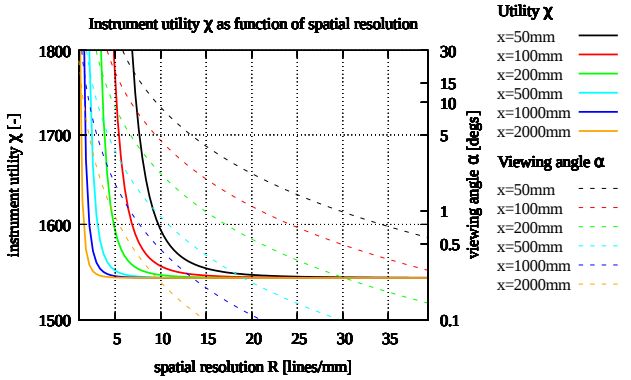

Figure 6: The utility measure $\chi(x,h)$ defined by eq. 20 (full lines) and the viewing angle α (dashed lines) in dependence on spatial resolution R and object distance x.

tween the rectangle and the camera, when the rectangle is rotated arbitrarily in a fixed angular range.

4.5. Survey of Existing BTF Setups

Existing designs of instruments for BTF measurements often state the spatial resolution purely depending on the sensor pixel size and sensor pixel resolution (i.e. the number of pixels on the sensor and the sensor area). The influence of diffraction is rarely discussed, even less so is the influence of the lens' aberrations. An analysis of the DoF is also mostly lacking, even though acquired images are taken of a sample highly tilted to the optical axis which requires a large DoF. In Table 1 we summarize the properties of the existing BTF measurement setups overviewed in Section 3 with an emphasis on the sample size h and the spatial resolution R. All of the listed setups use standard perspective imaging. As the input for our study we have taken the data from Table 6 of [SSW*14, page 7800] and [HF13, page 45, 46]. We also checked the original publications to complete and verify these input data.

For the listed measurement BTF setups we evaluate their maximum performance for a perfect lens without distortion using the eq. 19. The computed values are twofold: (a) given the sample size h, we compute the maximum spatial resolution R_{max} when the whole sample is viewed and vice versa, (b) given the sensor resolution in terms of number of pixels or specified in the paper determining the spatial resolution R we evaluate the maximum spatial size of the sample h_{max} that can be taken without visible blur.

From the analysis of existing data about measurement instruments we can deduce that some instruments were designed to fulfill the DoF limitation including the diffraction condition given the assumed sample size. For those instruments where the DoF is smaller than the specified sample size there are two boundary outcomes. Firstly, the blur due to diffraction can be prevailing when the aperture diameter is set small so as to fit the defocus limitation. Then the whole image is blurred evenly as would correspond to Figure 4(b) top. Secondly, the aperture can be set to the diffraction limit so the visible change of blur is due to defocus only. Then the taken images are sharpest in the center with the blur increasing towards the edges. There is a continuous space for setting the aperture between

Reference	max. tilt angle θ_{max} [°]	sample to camera distance x [mm]	max. sample size h [mm]	declared/ max. resolution R [$\frac{\text{lines}}{\text{mm}}$]	[1]max. spatial resolution R_{max} [$\frac{\text{lines}}{\text{mm}}$]	[2]max. sample size h_{max} [mm]
photogonioreflectometers						
[DNvGK97]	85	-	100	3.00	3.86	562.0
[SSK03]	75	1700	80	11.02	4.37	12.7
[SSK03]	75	1700	80	13.00	4.37	9.2
[KMBK03]	75	≈600	47	3.94	5.75	100.0
[RSK10]	75	1700	65	11.42	4.37	11.8
[HLZ10]	75	≈600	144	5.00	3.51	61.8
[FVH*13]	75	≈2000	44	42.17	5.91	0.8
[FVH*13]	75	≈2000	140	13.78	3.31	8.1
[FVK14]	75	≈240	30	13.39	7.21	8.6
kaleidoscopes						
[HP03]	65	615	58	3.35	4.41	148.0
[MTK*11]	75	–	50	9.84	5.55	15.9
[IRMS12]	-	–	210	0.71	2.76	391.0
array based setups						
[MMS*05]	75	650	105	9.25	2.52	18.0
[MMS*05]	75	650	105	17.72	2.52	4.9
[WMP*05]	75	≈1000	152	5.12	3.19	58.9
[SSWK13]	75	1000	100	7.48	3.94	27.5
[SSWK13]	75	1000	75	14.96	4.52	6.9
[KNRS13]	75	1000	46	5.00	5.79	61.7
[HHN*17a][3]	75	251	51	5.91	6.61	44.6

Table 1: The survey of existing BTF setups for size of sample and spatial resolution showing the maximum DoF of acquired images. [1] Maximum theoretical spatial resolution R_{max} is taken from eq. 19 by numerically finding inverse of function for maximum sample size h (4th column) that was described in the publications. [2] Maximum sample size h_{max} is computed directly from eq. 19 for declared spatial resolution R (5th column) in the published paper that corresponds to the native or used resolution of the camera sensor. [3] The setup [HHN*17a] was designed and computed for the pixel binning 4×4 at the camera sensor for square size 35.5 × 35.5mm with diagonal 51mm. The values in last two columns were calculated for a mean wavelength λ=550 nm.

these two boundary conditions for an unbalanced optical design, where the blur due to diffraction and the blur due to defocus are mixed together. Blur due to diffraction can prevail over the whole image or in its central region only.

As some previously published instruments for BTF measurement offer limited spatial resolution for maximum reported sample size, the question is the true output spatial resolution of the measured image datasets, even without considering the image quality deterioration caused by image processing needed for image rectification and alignment. To keep maximum quality of output images it is convenient to implement image processing by a simple homography transform combined with a suitable interpolation (at least bilinear) method from the input image.

For some practical choice of a sample size h such as a diameter of $h = 50$mm, which would provide sufficient visual richness and variety of measured spatially varying surface reflectance, the achievable spatial resolution is limited to only about 6 lines/mm

(i.e. 150 DPI) on the sample's surface, as shown in Figure 5. This can be considered as a severe obstacle, in particular for many practical applications of rendering close-ups of objects with BTF.

5. Tilted Object Imaging

In this section, we show a novel method taken from optics to resolve the problem with the required large DoF and/or spatial resolution for viewing planar objects. The method is applicable only to planar objects which perfectly fits the BTF measurement of flat material samples. To the best of our knowledge, this method has never been applied in the context of BTF data acquisition. Also, to our surprise, we have not found any use of the tilted imaging in the specialized conferences on computational photography and computer graphics although it is used in machine vision [Ste17, NKZN08, KA96].

For a standard perspective imaging a fixed-focus lens is focused at one distance, i.e., at one plane perpendicular to the optical axis. This restricts the spatial resolution for viewing a planar object at an angle, as we have shown in the previous section. To improve on spatial resolution for the same size of planar sample we suggest to use a custom made camera housing and optics that can take advantage of a special arrangement. For sharp imaging of a planar object at an angle to the optical axis we tilt the sensor as shown in Figure 7(a). This solution is called *tilted imaging* or *Scheimpflug imaging* [Lar65, Ray94, Mer93], first investigated by Jules Carpentier [Car01] and mathematically described by Theodor Scheimpflug [Sch04]. The rigorously formulated camera model with matrix notation for Scheimpflug imaging and calibration was published recently by Steger [Ste17].

In tilted imaging, to get a sharp image of a planar object this condition has to be fullfilled: for a single thin lens, three planes must share a common line: the object plane tilted at angle θ, the sensor plane tilted at angle θ' and the lens plane which is perpedicular to the optical axis. The Scheimpflug condition in the system is then expressed by computing the distance y_E for both triangles. We can derive the tilt angle of the sensor plane θ' with thin lens equation:

$$\begin{aligned} \tan\theta &= \frac{-x+f'}{y_E} \quad , \quad \tan\theta' = \frac{x'+f'}{y_E} \quad , \quad x' = \frac{-f'^2}{x} \\ y_E &= \frac{-x+f'}{\tan\theta} = \frac{x'+f'}{\tan\theta'} \quad \text{so we get for } \theta' : \\ \tan\theta' &= \frac{x'+f'}{-x+f'}\tan\theta = \frac{f'}{-x}\tan\theta \end{aligned} \tag{21}$$

The DoF of this tilted imaging system makes room for capturing an object which is not perfectly flat or is shifted along the optical axis. It follows from eq. 21 that for a large object distance $-x \gg f'$ the tilt of sensor plane θ' is a fraction of the tilt of object plane θ.

An analytical description of DoF of a Scheimpflug imaging system is given in [War08]. A comparison of a standard and a tilted sensor arrangement calculated in the Zemax software for the parameters of our instrument, using a paraxial lens is shown in Figure 7(b) and (c). In the following text we consider the design of the particular instrument presented in Section 2, with the object size $h = 51$mm, object to image distance $-x+x'+2f' = 260$mm. The chip size $w' \times h'$ is 7.065×5.299mm, the pixel size 3.45μm (Sony IMX265 chip). The aperture diameter D was set so as to balance the diffraction spot's and the geometrical spot's sizes. We can see in Figure 7(c) that for a tilted object only the center part is in focus, for pixel binning 2×2.

The tilted sensor arrangement solves the problem with DoF, but there is still another problem remaining: the variation in lateral magnification β defined by eq. 2. The object distance x varies with the position on the object, consequently, so does the lateral magnification β. A square object is then mapped as an isosceles trapezoid. This effect has to be compensated for during the image processing when rectifying and aligning the acquired images.

6. Anamorphic Imaging

Another consequence of viewing a tilted planar object is the shrinkage of the object. This effect is not related to the optical system. Seen at a high tilt angle θ from flat surface normal, a square becomes shorter at one side with the factor $\cos\theta$. The spatial resolution of the sample measured on the sample surface in horizontal and vertical directions will then differ. It would be useful to stretch the image in the tilt direction. We can hit two birds with one stone: the resolution in that direction can be restored as the image will fall over more pixels, and also the whole camera sensor area can be better utilized. This can be done by anamorphic optics [Rai89] often used in widescreen photography and cinematography. With a proper magnification in one direction, the resolution in the horizontal and vertical directions can be balanced. The image stretching is not a problem because the taken image must be postprocessed anyway to rectify and align the image with the other images.

Anamorphic optics can be a lens or a prism type. The lens type is shown in Figure 8. In both cases, the optics have a nonzero optical power in one plane and behaves like a plan-parallel plate in the perpendicular plane. The system is generally a telescope. The one we have used makes use of cylinder lenses, forming a Galilean telescope. We prefer cylinder lenses over prisms for two main reasons: the optical axis stays straight and the aberrations are smaller.

cam	object tilt	sensor tilt	anam. magn.β_a	f'_1 [mm]	f'_2 [mm]	f'_3 [mm]	f'_4 [mm]	$d_{2,3}$ [mm]
#1	$\theta_1 = 4.95°$	$\theta'_1 = 0°$	–	–	–	–	16.0	–
#2	$\theta_2 = 17.65°$	$\theta'_2 = 1.42°$	–	–	–	–	16.0	–
#3	$\theta_3 = 30.35°$	$\theta'_3 = 2.70°$	1.08	160	75.6	-70	12.5	5.6
#3	$\theta_4 = 43.05°$	$\theta'_4 = 4.30°$	1.20	160	60	-50	12.5	10.0
#5	$\theta_5 = 55.75°$	$\theta'_5 = 6.74°$	1.35	160	30	-22.2	12.5	7.8
#6	$\theta_6 = 68.45°$	$\theta'_6 = 11.52°$	1.35	160	30	-22.2	12.5	7.8

Table 2: Optics design for six cameras used in the extended setup with specification of optical elements as shown in Figure 10. The tilt angle θ_x of the x-th camera is for the middle angular position against a planar BTF sample.

7. Measurement Instrument with Enhanced Setup

Below, we describe the design of a BTF measurement instrument using an enhanced setup that utilizes a combination of Scheimpflug and anamorphic imaging as previously described. It builds on the base setup outlined in Figure 1 and detailed in [HHN*17a, HHN*17b]. The base setup achieved a spatial resolution of 150

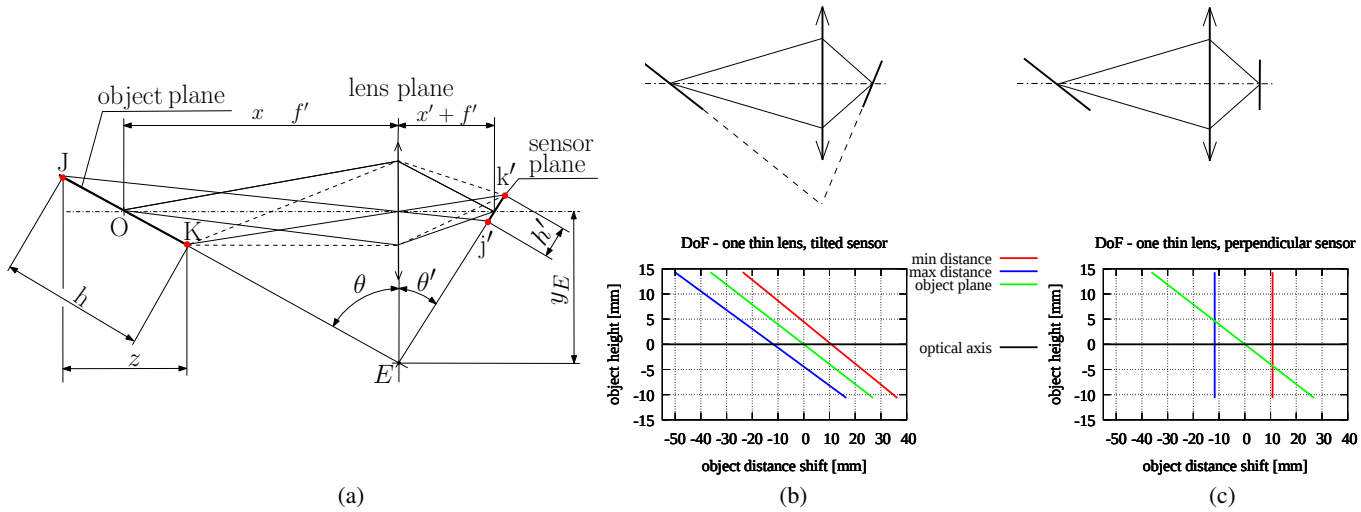

(a) (b) (c)

Figure 7: (a) Scheimpflug imaging principle for a thin lens viewing a tilted object at angle θ with the sensor plane tilted by angle θ′. Notation: x f' ... object distance from lens, $x'+f'$ ... image distance from lens, J ... top point of the planar object, O ... on-axis point, K ... bottom point of the planar object, h ... object sample size, h' ... size of sensor plane. (b) DoF of Scheimpflug imaging system with a single lens. Object is tilted against optical axis at angle 68°. (c) DoF of standard perspective imaging system with a single lens. The calculation of DoF was carried out for the base setup with pixel binning 2×2 and paraxial optics. The object to sensor distance and on-axis lateral magnification is the same for both cases. The DoF is measured from on-axis object point O. Green lines are the object positions, red and blue lines limits the range of sharp image.

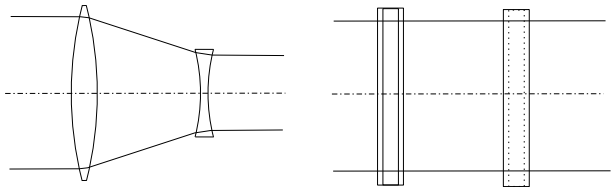

(a) (b)

Figure 8: An anamorphic attachment implemented using Galilean telescope made of two cylindrical lenses, first of them convex and second one concave. (a) view from a side, (b) view from top.

DPI for a sample size $35.5 \times 35.5\text{mm}^2$ (circle diameter 51mm) and was designed for pixel binning 4×4.

For the extended setup we use different cameras than those in the base setup. More importantly, all the lenses for the six cameras are designed specifically for BTF measurement at the required tilt angles θ as given in Table 2. This way we improve the spatial resolution of measurement by a factor of 1.90 (from 150 to 286 DPI). Each of the six cameras in the instrument looks at the object at a different tilt angle θ and therefore has unique optics. The top camera (#1 with central tilt angle $\theta = 4.95°$) is almost perpendicular to the surface normal and uses standard perspective imaging. The second camera (#2 with $\theta = 17.65°$) optics utilizes only Scheimpflug imaging. For the rest of the cameras #3 to #6 with higher tilt angles θ against the measured sample we stretch the image across the shorter side using an anamorphic attachment and we also use Scheimpflug imaging as outlined in Figure 10(a). For the lens design, it has to be considered that all cameras change their tilt angle θ to a surface normal in a limited range of ±6.25° around their center tilt position and the DoF has to be sufficient at that range over the whole planar sample. The lenses were designed for the center tilt position and rechecked for both extreme tilt positions.

The anamorphic attachment introduced in the previous section works correctly only if placed in a beam of parallel rays. For that reason we added another lens in front of the whole system. This lens has its front focus at the on-axis point of the sample. The resulting optical system is shown in Figure 10(b). The sample is projected by the first lens to infinity, then magnified by the anamorphic telescope and finally mapped onto the sensor by the camera lens. Lateral magnifications in the x and y directions are then given by

$$\beta_x = \frac{f_1'}{f_4'} \qquad \beta_y = \frac{f_1'}{f_4'}\frac{f_2'}{f_3'} \tag{22}$$

We can derive the necessary magnification β_a of the anamorphic attachment so that the image falls over the whole sensor as:

$$\beta_a = \frac{h'}{h}\frac{\cos\theta'}{\cos\theta}\frac{f_4'}{f_1'} \tag{23}$$

The sensor tilt cannot be thought of as an increase of the DoF, this arrangement just makes the image sharp for a particular planar object tilt. It does not mean the DoF is the whole depth $z = h\sin\theta$. We calculated the DoF for the design with a Galilean cylindrical telescope in the software Zemax, using paraxial lenses, see Figure 10(c). Note that even for perfect lenses, the spot sizes for the object edges (the points J and K in Figure 7) are slightly bigger than the pixel size. The result is shown for the worst case, camera #6, in Figure 13 where the chromatic aberrations are shown to be less than 1 pixel in the worst case. The DoF for these boundary points is then zero.

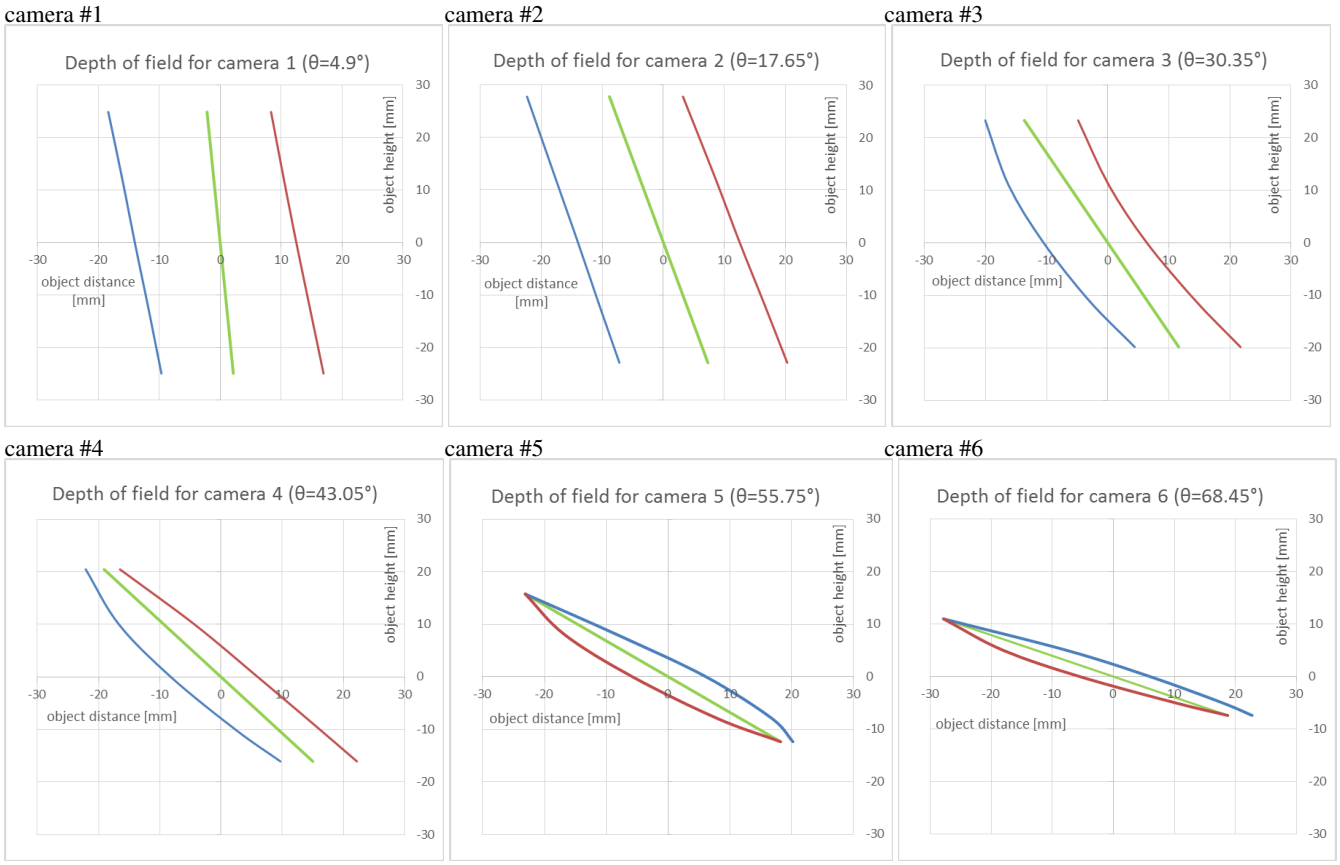

Figure 9: The DoF calculated in the software Zemax as a distance from the object's central position for six cameras calculated for spatial resolution $R = 286$ DPI, camera sensor pixel binning 2×2. Green lines are the planar object positions, red and blue lines are the minimum and maximum object point's shifts to remain sharp in image plane on detector.

8. Results

We describe the building of the instrument, the measurement and evaluation of acquired data and finally we discuss the limitations and pros and cons of the proposed method.

8.1. Extended setup build

We have built a BTF measurement instrument mechanically similar to the base setup [HHN*17a, HHN*17b] and equipped it with the proposed lens design. There are several important differences between the base setup and the newly built extended setup. The base setup used six cameras PointGrey FL3-U3-32S2C-CS (3.2 MPixels, pixel size 2.5μm, pixel binning 4×4) and 139 LED modules. The extended setup uses a different camera model, PointGrey CM3-U3-31S4C-CS, (3.2 MPixels, pixel size 3.45μm) and is designed specifically for pixel binning 2×2. Also, the extended setup uses in total 144 LED modules, 139 on the skeleton and 5 between the cameras, distributed differently on the hemispherical skeleton than in the base setup. Both the base setup and extended setup use a hemispherical skeleton of the same radius.

The mechanical parts for the cameras were designed, machined, assembled and adjusted according to the optics design described in Table 2. We used a combination of off-the-shelf lenses, different for each camera. The custom camera housing for cameras #2 to #5 was fabricated. Off-the-shelf optical components from Edmund Optics and Thorlabs were used (the specification in the supplementary).

A solid drawing of the arrangement used for the camera #5 is shown in Figure 11 and a photograph of the final assembly of the cameras is shown in Figure 12. The lens Fujinon C-mount 16mm was used for cameras #1 and #2, the lens Fujinon C-mount 12.5mm was used for cameras #3 to #6. To avoid glare all the lenses used for the anamorphic attachments are antireflex coated for visible light and the mechanical parts of the camera housing are black-anodized. The whole assembled extended setup is shown in Figure 14 from two sides, with the cover unmounted.

The anamorphic magnification for the camera #6 should optimally be 2.0, but this turned out to be too demanding for real lenses according to our initial experiments of making such imaging and its optical adjustment. We therefore used a smaller magnification β_a to make the spot sizes acceptable. The DoF for all cameras are shown in Figure 9, again calculated in the software Zemax.

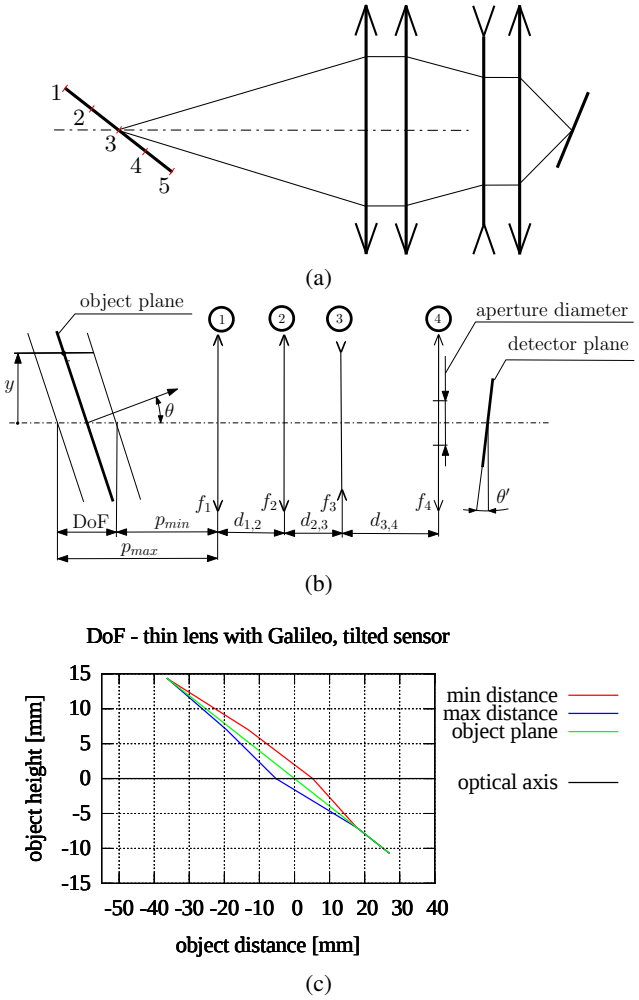

Figure 10: Scheimpflug imaging with anamorphic attachment, (a) the scheme for derivation of magnification with five denoted points marked 1 to 5 on the object that are referred in Figure 13, (b) the proposed optics combining Scheimpflug imaging and anamorphic imaging with cylindrical lenses used for camera #4 to #6. ① is a doublet lens that serves to collimate an input beam, ② is a plano-convex cylindrical lens, ③ is a plano-concave cylindrical lens, ④ is a standard imaging lens in front of a camera. ② and ③ form anamorphic attachment, (c) calculated DoF for camera #6 for the tilt angle $\theta = 68.45^\circ$.

8.2. Measurement and evaluation

The measurement procedure was the same as for the base setup, i.e. it used 120 camera positions for 20 rotations of the servo motor. As the number of images for one camera position corresponds to the number of LEDs, i.e. 144, the measurement produced 120×144=17280 images. The measurement time was optimized to 860 seconds. The image rectification procedure is based on the algorithm in [HHN*17a], only the camera model had to be changed to account for the combination of Scheimpflug imaging and anamorphic attachment. The anamorphic imaging corresponds to the change of the lateral field of view for the camera in the software and unlike perspective imaging it cannot be implemented by a simple homogeneous matrix transform. We provide the algorithmic camera model based on the geometric optics verified against the measured data in the supplementary.

The base setup used pixel binning 4×4 to get the spatial resolution of 150 DPI. The extended setup requires pixel binning 2×2 as the cameras move along a circular arc in the range $\pm 6.25^\circ$. This results in a spatial resolution of 11.3 lines per mm (286 DPI). We measured three identical material samples with the optics from the base setup and also with the extended setup to allow for the mutual side-by-side comparison of the acquired images. The example images for the material *basketball* from MAM 2014 Sample Set [Rus14] are shown in Figure 15 including three close-ups of the boundary regions of the measured sample. The measured images of the other two materials with sharp features (*silver-gold* and *sand-coarse*) are shown in the supplementary. To have the same conditions, the images were taken with binning set to 2×2 for both arrangements of optics from the base setup and extended setup. In addition to the material sample features, we used a 600 DPI silkscreen printed circular marker sticker with a black and white radial chequerboard pattern. So the amount of blur can be evaluated on the marker sticker as well. We can observe how the spatial resolution and the magnification of the sample improved with the new optical design when compared to the base setup. As the cameras for the base setup and the extended setup are different, the color tint of the images from the two setups is sligtly different even when the illumination direction from the LED module was the same.

We processed the measured data from the extended setup to BTFs by image rectification. We have implemented two rendering applications, one offline as a plugin to Mitsuba renderer [Jak10] and the second one as an OpenGL interactive renderer with shader in GLSL, running at 60 FPS. The compression BTF algorithm was not used as the whole dataset for one BTF sample fitted into the memory on a GPU card. We used both point lighting and environment map illumination to study the quality of measurements from the extended setup. The rendered images for the six material samples measured by the instrument with the new optics as described above (four physical samples from MAM 2014 Sample Set [Rus14] and two other samples) and four 3D objects for point light illumination (allows for better visual inspection) are shown in Figure 16. For completeness we provide in the supplementary material the preview for all the measurements plus 12 images for the sample *basketball*.

8.3. Discussion and limitations

There are other possible solutions to increase DoF called *extended DOF* such as the methods in [NKZN08, LRLCCY*17] and references therein. In principle, it is (a) possible to refocus the camera and assemble the image from two or more individually taken images focused at different object distances or (b) vary the aperture and get several images and apply image processing to composite a single image. However, the change of optical elements and acquisition of more images requires time and alters the lateral magnification of individual images. High quality varifocal lenses are bulky, expensive and heavy. Another method could be to use software based deblurring as proposed by Nam et al. [NLW*16] for

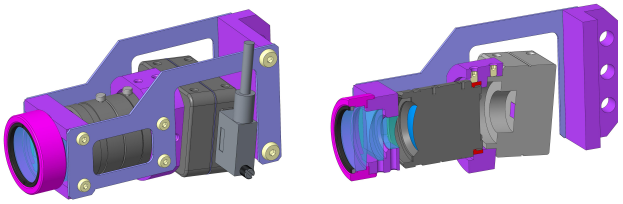

(a) (b)

Figure 11: CAD model of camera #5 (a) whole camera unit assembled consisting of Fujinon lens, two cylindrical lenses and front dublet convex lens, (b) sectional view of the camera unit. The camera sensor tilt angle $\theta = 6.74^\circ$.

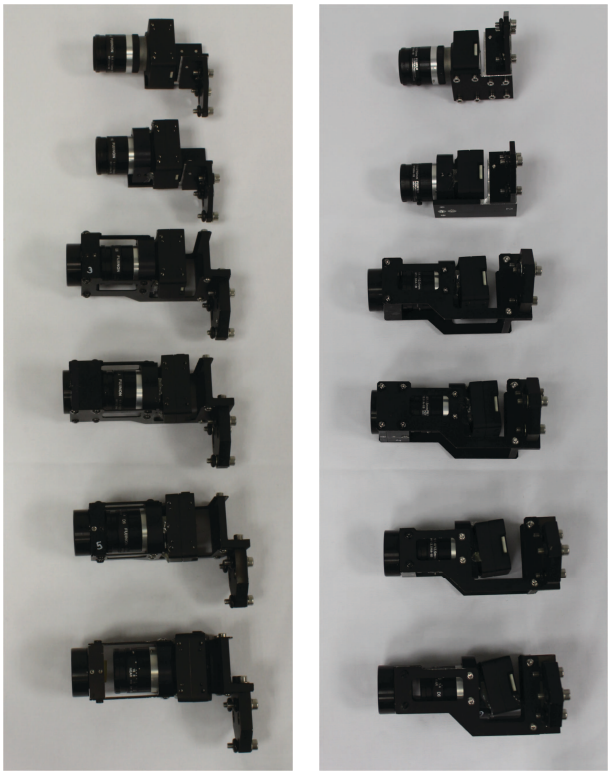

Figure 12: Photographs of assembled camera units with the proposed optics, camera #1 at the top, camera #6 (biggest tilt angle) at the bottom. The cameras #2 to #6 use custom optics. (a) top view, (b) side view with visible tilt of sensors to optical axes.

microscale flat objects' capture. However, the software deblurring is useful only for larger blur scales and it cannot give a perfect reconstruction comparable to the custom design optics as presented here. For smaller blur spots close to 2×2 pixels as in our case the image quality improvement by such software deblurring methods is negligible. Though hardware solutions to alleviate the image processing have appeared recently [LRLCCY*17], such solutions are expensive, bulky and heavy and require more time for taking images than is acceptable for surface reflectance measurements, as thousands of images have to be taken.

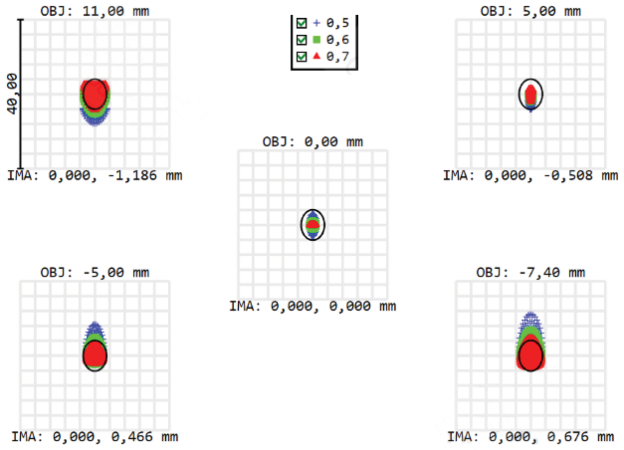

Figure 13: Zemax software simulation for camera #6 (snapshot from software). The geometrical spots due to lens aberrations for three wavelengths and five points on the object plane as depicted in Figure 10 (a). The spot radii for points #1 to #5 are 3.77, 1.54, 1.06, 2.80, 3.76μm, respectively. The wavelengths are 500nm, 600nm, 700nm denoted in the image by different colours.

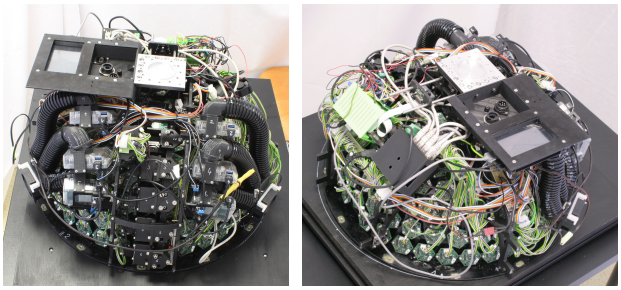

Figure 14: Photographs of assembled measurement instrument from two sides, with the cover unmounted. The left image shows the camera units from Figure 12 along meridian in the middle bottom. The parts of the instrument are detailed in [HHN*17a].

For fixed setups with a predefined tilt angle of the camera to the measured planar sample such as [MBK05, SSWK13] the Scheimpflug imaging can achieve a full utilization of the camera sensor, supposing that high quality lenses are used. In our case the tilt of cameras against the sample normal is varied by $\pm 6.25^\circ$ so the design requires pixel binning 2×2. For some setups such as kaleidoscopic [HP03, IRMS12] or photogonioreflectometric [RSK10, SSK03, HM12] ones, Scheimpflug imaging cannot be used as either the tilt changes greatly across the sample and does not form a plane, or the tilt changes with the camera repositioning.

Scheimpflug imaging can be successfully applied to setups where the tilt of cameras against the sample is fixed or changes only within a limited range, as in our design. Note that the equation 19 derived in this paper does not address the Scheimpflug imaging. As very recently pointed out in [ZG18] the use of Scheimpflug imaging may result in geometric distortions for larger tilt angles of camera sensor to optical axis. This can be compensated for either by custom freeform optics or by the use of precomputed lookup tables

during image processing. As the maximum tilt angle of the camera sensor is relatively small in our case (11.52° for camera #6 and only 6.74° for camera #5, following from eq. 21), the object distance x is much larger than focal length f', these aberrations are small for the extended setup.

The method of Scheimpflug imaging is relatively simple to design and implement even for a non-expert using eq. 21. However, when combined with an anamorphic attachment as described for cameras #3 to #6, it requires a custom optical design in specialized software such as Zemax, precisely machined metal parts and a careful adjustment of the optics. It can be difficult or even impossible to implement this successfully without appropriate optics equipment and sufficient experience in optics adjustment.

9. Conclusions

In our paper we addressed the depth of field for computer graphics acquisition applications in the context of BTF measurement. We focused our analysis on surface reflectance measurement of a planar material sample. From our analysis we derived that for a planar object measured at different tilt angles with the use of perspective imaging, the spatial resolution and the size of the object are strongly interdependent due to the depth of field being limited by diffraction. We provided a new explicit formula for optical design of perspective imaging that can be used in a variety of technical applications. Utilizing this formula we surveyed the properties of existing BTF measurement setups. To improve on the spatial resolution, we proposed a novel solution which utilizes Scheimpflug imaging, optionally combined with an anamorphic attachment. We used this to build a new BTF measurement prototype that is portable and allows for measuring on site.

Our analysis of the limited depth of field versus spatial resolution of a fixed-focus lens is valid for all imaging applications with standard perspective imaging used in computer graphics, computer vision and other imaging application areas for a simple thin lens model. The proposed use of Scheimpflug imaging can provide a convenient solution for camera arrays in BTF and SVBRDF measurement setups where cameras are fixed or move only in a small limited range of tilt with respect to a flat object normal.

In the future, we would like to extend the presented instrument to allow for a spectral measurement to approach the ultimate goal for BTF measurement – a fully portable solution with the maximum spatial resolution and a spectral acquisition that allows BTF measurement on site.

Acknowledgement

This work was partially supported by the Czech Science Foundation (GACR) of the Czech Republic, under research project number GA14-19213S. The first author acknowledges the support of the OP VVV MEYES funded project CZ.02.1.01/0.0/0.0/16_019/0000765 "Research Center for Informatics".

References

[Air34] AIRY G. B.: On the Diffraction of an Object-glass with Circular Aperture. *Transactions of the Cambridge Philosophical Society 5* (Nov. 1834), 283–291. URL: https://archive.org/details/transactionsofca05camb. 5

[AWL13] AITTALA M., WEYRICH T., LEHTINEN J.: Practical SVBRDF Capture in the Frequency Domain. *ACM Trans. Graph. 32*, 4 (july 2013), 110:1–110:12. URL: http://doi.acm.org/10.1145/2461912.2461978. 3

[BEWW*08] BEN-EZRA M., WANG J., WILBURN B., LI X., MA L.: An LED-only BRDF measurement device. In *IEEE Conference on Computer Vision and Pattern Recognition, CVPR 2008.* (June 2008), IEEE Computer Society, pp. 1–8. URL: http://dx.doi.org/10.1109/CVPR.2008.4587766. 4

[BK08] BARSKY B. A., KOSLOFF T. J.: Algorithms for rendering depth of field effects in computer graphics. In *Proceedings of the 12th WSEAS International Conference on Computers* (Stevens Point, Wisconsin, USA, 2008), ICCOMP'08, pp. 999–1010. URL: http://dl.acm.org/citation.cfm?id=1513605.1513775.

[Car01] CARPENTIER J.: Improvements in enlarging or like cameras, 1901. British Patent no. 1139(1901). 9

[Dan01] DANA K.: BRDF/BTF Measurement Device. In *Computer Vision, 2001. ICCV 2001. Proceedings. Eighth IEEE International Conference on* (2001), vol. 2, pp. 460–466 vol.2. URL: http://dx.doi.org/10.1109/ICCV.2001.937661. 3

[Dan16] DANA K. J.: Capturing Computational Appearance: More than meets the eye. *IEEE Signal Processing Magazine 33*, 5 (Sept 2016), 70–80. URL: http://dx.doi.org/10.1109/MSP.2016.2580179. 3

[DD08] DERENIAK E., DERENIAK T.: *Geometrical and Trigonometric Optics*. Cambridge University Press, 2008. ISBN 9780521887465. 4, 7

[DHT*00] DEBEVEC P., HAWKINS T., TCHOU C., DUIKER H.-P., SAROKIN W., SAGAR M.: Acquiring the Reflectance Field of a Human Face. In *Proceedings of SIGGRAPH'00* (New York, NY, USA, 2000) ACM Press/Addison-Wesley Publishing Co., pp. 145–156. URL: http://dx.doi.org/10.1145/344779.344855. 4

[DNvGK97] DANA K. J., NAYAR S. K., VAN GINNEKEN B., KOENDERINK J. J.: Reflectance and texture of real-world surfaces. In *IEEE Conference on Computer Vision and Pattern Recognition, CVPR 1997.* (Jun 1997), pp. 151–157. http://dx.doi.org/10.1109/CVPR.1997.609313. 3, 8

[DVGNK99] DANA K., VAN-GINNEKEN B., NAYAR S., KOENDERINK J.: Reflectance and Texture of Real World Surfaces. *ACM Trans. Graph. 18*, 1 (Jan 1999), 1–34. 2, 3

[FVH*13] FILIP J., VÁVRA R., HAINDL M., ŽID P., KRUPIČKA M., HAVRAN V.: BRDF Slices: Accurate Adaptive Anisotropic Appearance Acquisition. In *IEEE Conference on Computer Vision and Pattern Recognition, CVPR 2013.* (June 2013), pp. 4321–4326. URL: http://btf.utia.cas.cz/?brdf_dwn. 8

[FVK14] FILIP J., VÁVRA R., KRUPIČKA M.: Rapid Material Appearance Acquisition Using Consumer Hardware. *Sensors 14*, 10 (2014), 19785–19805. URL: http://doi.org/10.3390/s141019785. 3, 4, 8

[HD14] HANIKA J., DACHSBACHER C.: Efficient Monte Carlo Rendering with Realistic Lenses. *Computer Graphics Forum 33*, 2 (2014), 323–332. URL: http://dx.doi.org/10.1111/cgf.12301. 4

[HF13] HAINDL M., FILIP J.: *Visual Texture*. Advances in Computer Vision and Pattern Recognition. Springer-Verlag, London, 2013. URL: http://www.springer.com/computer/image+processing/book/978-1-4471-4901-9. 3, 8

[HHN*17a] HAVRAN V., HOSEK J., NEMCOVA S., CAP J., BITTNER J.: Lightdrum – Portable Light Stage for Accurate BTF Measurement on Site. *Sensors 17*, 3 (2017). URL: http://doi.org/10.3390/s17030423. 3, 4, 8, 9, 11, 12, 13, 15

[HHN*17b] HOSEK J., HAVRAN V., NEMCOVA S., BITTNER J., CAP J.: Optomechanical design of a portable compact bidirectional texture function measurement instrument. *Appl. Opt. 56*, 4 (Feb 2017), 1183–1193. URL: http://doi.org/10.1364/AO.56.001183. 3, 4, 9, 11, 15

[HLZ10] HOLROYD M., LAWRENCE J., ZICKLER T.: A Coaxial Optical Scanner for Synchronous Acquisition of 3D Geometry and Surface Reflectance. *ACM Trans. Graph. 29*, 4 (July 2010), 99:1–99:12. URL: http://doi.acm.org/10.1145/1778765.1778836. 8

[HM12] HAINDL M. FILIP J. V. R.: Digital Material Appearance: The

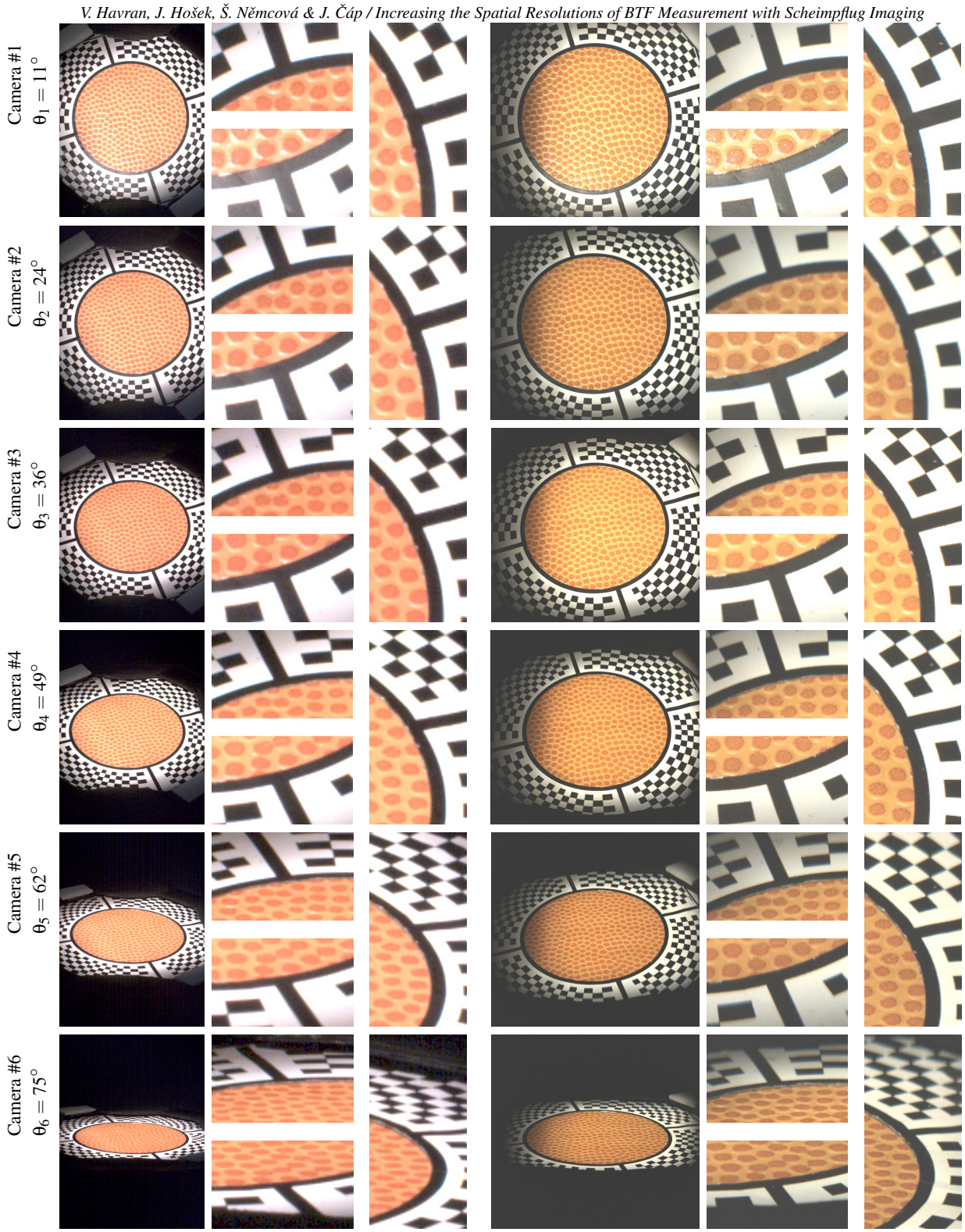

Figure 15: Material *basketball* from [Rus14]. The images taken for binning 2×2 pixels on camera sensor for base setup and extended setup using the same direction of illumination for cameras #1 to #6. The hole with the measured sample has diameter 51mm. Base setup [HHN*17a, HHN*17b], 150 DPI, (a) a full image, (b) close-ups of the middle top and middle bottom parts from the image, (c) close-up for the right part of the image. An extended setup with Scheimpflug imaging and anamorphic attachment, 286 DPI, (d) a full image, (e) close-ups of the middle top and middle bottom parts from the image, (f) close-up for the right part of the image.

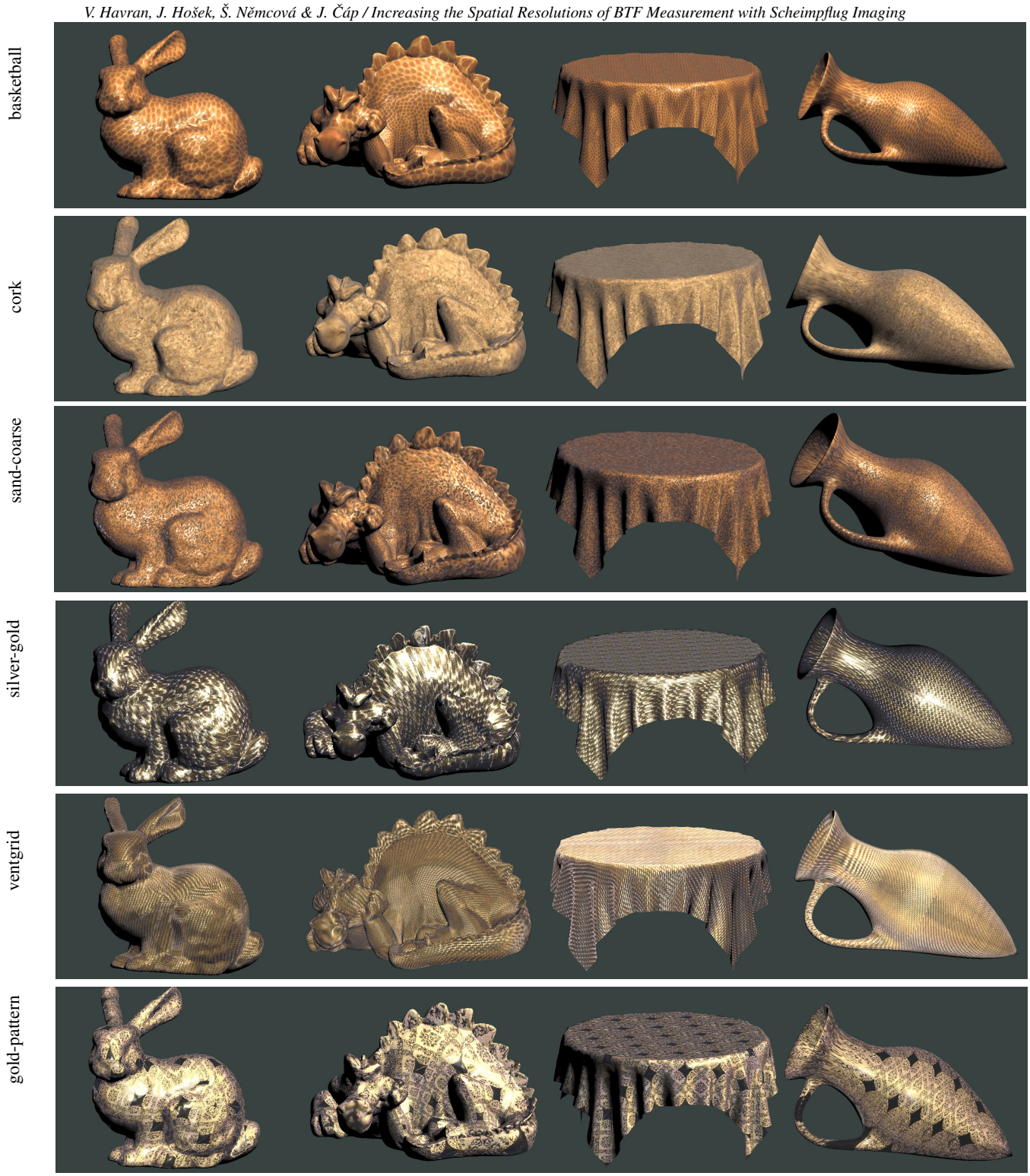

Figure 16: A set of 24 example images rendered by an interactive OpenGL application for six sample materials *basketball*, *cork*, *sand-coarse*, *silver-gold* from [Rus14], and for two other materials with sharp features. The BTF data were measured by the proposed instrument with Scheimpflug imaging. Four 3D objects are used, camera and light source positions for rendering little vary among rows as the images were taken as snapshot in an interactive OpenGL application. The texture parameterization over the object's surface vary for example for dragon model so it is possible to see the quality of the captured data at different scale. No BTF compression is used to show the BTF data as sharp as possible. The illumination used for rendering the images is one point light source.

Curse of Tera-Bytes. *ERCIM News*, 90 (2012), 49–50. 13

[HP03] HAN J. Y., PERLIN K.: Measuring Bidirectional Texture Reflectance with a Kaleidoscope. *ACM Trans. Graph. 22*, 3 (july 2003), 741–748. URL: http://doi.acm.org/10.1145/882262.882341. 4, 8, 13

[IRMS12] IHRKE I., RESHETOUSKI I., MANAKOV A., SEIDEL H.-P.: Three-Dimensional Kaleidoscopic Imaging. In *Computational Optical Sensing and Imaging* (2012), Optical Society of America, paper CTu4B.8. 8, 13

[Jak10] JAKOB W.: Mitsuba renderer, 2010. URL: http://www.mitsuba-renderer.org. 12

[KA96] KRISHNAN A., AHUJA N.: Range estimation from focus using a non-frontal imaging camera. *International Journal of Computer Vision 20*, 3 (Dec 1996), 169–185. URL: http://dx.doi.org/10.1007/BF00208718. 9

[KMBK03] KOUDELKA M. L., MAGDA S., BELHUMEUR P. N., KRIEGMAN D. J.: Acquisition, Compression, and Synthesis of Bidirectional Texture Functions. In *In ICCV 03 Workshop on Texture Analysis and Synthesis* (2003), pp. 47–52. 8

[KMH95] KOLB C., MITCHELL D., HANRAHAN P.: A realistic camera model for computer graphics. In *Proceedings of the 22Nd Annual Conference on Computer Graphics and Interactive Techniques* (New York, NY, USA, 1995), SIGGRAPH '95, ACM, pp. 317–324. URL: http://doi.acm.org/10.1145/218380.218463. 4

[KNRS13] KOHLER J., NOLL T., REIS G., STRICKER D.: A full-spherical device for simultaneous geometry and reflectance acquisition. In *Applications of Computer Vision (WACV), 2013 IEEE Workshop on* (Jan 2013), pp. 355–362. URL: http://dx.doi.org/10.1109/WACV.2013.6475040. 4, 8

[Lar65] LARMORE L.: *Introduction to Photographic Principles*. Dover Publications, 1965. 9

[LRLCCY*17] LOPEZ-RAMIREZ M., LEDESMA-CARRILLO L., CABAL-YEPEZ E., BOTELLA G., RODRIGUEZ-DONATE C., LEDESMA S.: FPGA-based methodology for depth-of-field extension in a single image. *Digital Signal Processing 70* (2017), 14 – 23. URL: https://doi.org/10.1016/j.dsp.2017.07.014. 12, 13

[MBK05] MÜLLER G., BENDELS G. H., KLEIN R.: Rapid Synchronous Acquisition of Geometry and BTF for Cultural Heritage Artefacts. In *The 6th International Symposium on Virtual Reality, Archaeology and Cultural Heritage (VAST)* (Nov. 2005), Eurographics Association, pp. 13–20. 13

[Mer93] MERKLINGER H.: *Focusing the View Camera: A Scientific Way to Focus the View Camera and Estimate Depth of Field*. H.M. Merklinger, 1993. 9

[MGW01] MALZBENDER T., GELB D., WOLTERS H.: Polynomial texture maps. In *Proceedings of the 28th annual conference on Computer graphics and interactive techniques* (New York, NY, USA, 2001), SIGGRAPH '01, ACM, pp. 519–528. URL: http://doi.acm.org/10.1145/383259.383320. 4

[MMS*05] MÜLLER G., MESETH J., SATTLER M., SARLETTE R., KLEIN R.: Acquisition, Synthesis, and Rendering of Bidirectional Texture Functions. *Computer Graphics Forum 24*, 1 (2005), 83–109. URL: http://dx.doi.org/10.1111/j.1467-8659.2005.00830.x. 4, 8

[MTK*11] MUKAIGAWA Y., TAGAWA S., KIM J., RASKAR R., MATSUSHITA Y., YAGI Y.: *Hemispherical Confocal Imaging Using Turtleback Reflector*. Springer Berlin Heidelberg, Berlin, Heidelberg, 2011, pp. 336–349. URL: http://dx.doi.org/10.1007/978-3-642-19315-6_26. 8

[NKZN08] NAGAHARA H., KUTHIRUMMAL S., ZHOU C., NAYAR S. K.: Flexible Depth of Field Photography. In *Computer Vision – ECCV 2008* (Berlin, Heidelberg, 2008), Forsyth D., Torr P., Zisserman A., (Eds.), Springer Berlin Heidelberg, pp. 60–73. 9, 12

[NLW*16] NAM G., LEE J. H., WU H., GUTIERREZ D., KIM M. H.: Simultaneous Acquisition of Microscale Reflectance and Normals. *ACM Trans. Graph. 35*, 6 (Nov. 2016), 185:1–185:11. http://doi.acm.org/10.1145/2980179.2980220. 12

[NRH*77] NICODEMUS F. E., RICHMOND J. C., HSIA J. J., GINSBERG I. W., LIMPERIS T.: *Geometric Considerations and Nomenclature for Reflectance*. Monograph 161, National Bureau of Standards (US), October 1977. 2

[PC81] POTMESIL M., CHAKRAVARTY I.: A Lens and Aperture Camera Model for Synthetic Image Generation. *SIGGRAPH Comput. Graph. 15*, 3 (Aug. 1981), 297–305. URL: http://doi.acm.org/10.1145/965161.806818. 5

[Rai89] RAINSDON M. D.: *An anamorphic imaging model to correct geometric distortion in planar holographic stereograms*. PhD thesis, Rochester Institute of Technology, 1989. 9

[Ray94] RAY S.: *Applied Photographic Optics: Lenses and Optical Systems for Photography, Film, Video, and Electronic Imaging*. Focal Press, 1994. 9

[RPG16] RIVIERE J., PEERS P., GHOSH A.: Mobile Surface Reflectometry. *Computer Graphics Forum 35*, 1 (2016), 191–202. URL: http://dx.doi.org/10.1111/cgf.12719. 3

[RSK10] RUMP M., SARLETTE R., KLEIN R.: Groundtruth Data for Multispectral Bidirectional Texture Functions. In *CGIV 2010* (June 2010), Society for Imaging Science and Technology, pp. 326–330. 8, 13

[Rus14] RUSHMEIER H.: The MAM2014 Sample Set. In *Eurographics Workshop on Material Appearance Modeling* (2014), Klein R., Rushmeier H., (Eds.). URL: http://dx.doi.org/10.2312/mam.20141297. 12, 15, 16

[Sch04] SCHEIMPFLUG T.: Improved method and apparatus for systematic alteration or distortion of plane pictures and images by means of lenses and mirrors for photography and for other purposes, 1904. British Patent no. 1196(1904). 9

[SSK03] SATTLER M., SARLETTE R., KLEIN R.: Efficient and Realistic Visualization of Cloth. In *Proceedings of the 14th Eurographics workshop on Rendering* (Aire-la-Ville, Switzerland, 2003), EGRW '03, pp. 167–177. 8, 13

[SSW*14] SCHWARTZ C., SARLETTE R., WEINMANN M., RUMP M., KLEIN R.: Design and Implementation of Practical Bidirectional Texture Function Measurement Devices Focusing on the Developments at the University of Bonn. *Sensors 14*, 5 (2014), 7753–7819. URL: http://dx.doi.org/10.3390/s140507753. 3, 4, 8

[SSWK13] SCHWARTZ C., SARLETTE R., WEINMANN M., KLEIN R.: DOME II: A Parallelized BTF Acquisition System. In *Eurographics Workshop on Material Appearance Modeling* (2013), Klein R., Rushmeier H., (Eds.), pp. 25–31. URL: http://dx.doi.org/10.2312/MAM.MAM2013.025-031. 4, 8, 13

[Ste17] STEGER C.: A Comprehensive and Versatile Camera Model for Cameras with Tilt Lenses. *International Journal of Computer Vision*, Vol. 123, Issue 2 (Jun 2017), 121–159. URL: https://doi.org/10.1007/s11263-016-0964-8. 9

[War08] WAREHAM L.: Tilt and Shift Lenses, 2008. URL: http://www.zen20934.zen.co.uk/photography/tiltshift.htm. 9

[WK15] WEINMANN M., KLEIN R.: Advances in Geometry and Reflectance Acquisition (Course Notes). In *SIGGRAPH Asia 2015 Courses* (New York, NY, USA, 2015), SA'15, ACM, pp. 1:1–1:71. URL: http://doi.acm.org/10.1145/2818143.2818165. 3

[WMP*05] WEYRICH T., MATUSIK W., PFISTER H., NGAN A., GROSS M.: *Measuring Skin Reflectance and Subsurface Scattering*. Tech. Rep. TR2005-046, MERL - Mitsubishi Electric Research Laboratories, Cambridge, MA 02139, July 2005. URL: http://www.merl.com/publications/TR2005-046/. 8

[XDPT16] XIA R., DONG Y., PEERS P., TONG X.: Recovering Shape and Spatially-Varying Surface Reflectance under Unknown Illumination. *ACM Trans. Graph. 35*, 6 (Nov. 2016). URL: https://doi.org/10.1145/2980179.2980248. 3

[XR16] X-RITE: Tac 7 scanner, 2016. Accessed at 25th April 2017. URL: http://www.xrite.com/categories/Apperance/tac7. 3

[ZCD*16] ZHOU Z., CHEN G., DONG Y., WIPF D., YU Y., SNYDER J., TONG X.: Sparse-as-Possible SVBRDF Acquisition. *ACM Trans. Graph. 35*, 6 (Nov. 2016), 189:1–189:12. URL: http://doi.acm.org/10.1145/2980179.2980247. 3

[ZG18] ZHONG Y., GROSS H.: Improvement of Scheimpflug systems with freeform surfaces. *Appl. Opt. 57*, 6 (Feb 2018), 1482–1491. URL: http://dx.doi.org/10.1364/AO.57.001482. 13